THE JOURNAL OF PHYSICAL CHEMISTRY C

Article

pubs.acs.org/JPCC

The Effects of Crystal Structure and Electronic Structure on Photocatalytic H_2 Evolution and CO_2 Reduction over Two Phases of Perovskite-Structured $NaNbO_3$

Peng Li,[†,‡,§] Shuxin Ouyang,[‡] Guangcheng Xi,[‡] Tetsuya Kako,[†,‡] and Jinhua Ye*[,†,‡,§,∥]

[†]Department of Chemistry, Graduate School of Science, Hokkaido University, Sapporo, Japan

[‡]Environmental Remediation Materials Unit, National Institute for Materials Science (NIMS), 1-2-1 Sengen, Tsukuba, Ibaraki 305-0047, Japan

[§]International Center for Materials Nanoarchitectonics (WPI-MANA), National Institute for Materials Science (NIMS), 1-2-1 Sengen, Tsukuba, Ibaraki, Japan

[∥]TU-NIMS Joint Research Center, School of Materials Science and Engineering, Tianjin University, 92 Weijin Road, Nankai District, Tiajin, People's Republic of China

Supporting Information

ABSTRACT: Cubic and orthorhombic $NaNbO_3$ were fabricated to study the effects of crystal structure and electronic structure on the photocatalytic activities in detail. The samples were characterized by X-ray diffraction, field emission transmission electron microscopy, high-resolution transmission electron microscopy, UV−visible absorption spectroscopy, and X-ray photoelectron spectroscopy. The photocatalytic activities of the two phases of $NaNbO_3$ have been assessed by H_2 evolution from aqueous methanol solution and CO_2 photoreduction in gas phase. The photocatalytic H_2 evolution and CO_2 reduction activities over cubic $NaNbO_3$ were nearly twice of those over orthorhombic $NaNbO_3$. The first-principles calculation reveals that the higher activity over cubic $NaNbO_3$ can be attributed to its unique electronic structure, which is beneficial for electron excitation and transfer.

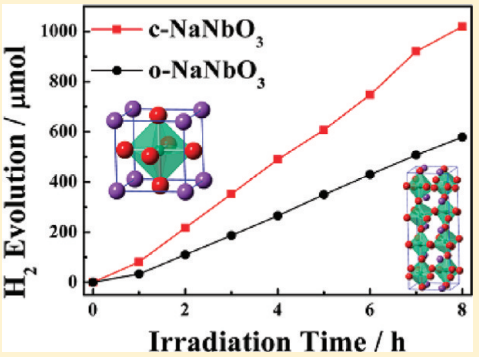

INTRODUCTION

As the fossil fuels have limitations in availability, a new source that can provide abundant and maintainable energy must be developed.[1,2] For the past decades, photocatalysis has been developed as a candidate that can supply a renewable, unlimited, and environmentally friendly energy source to solve the energy crisis.[3,4] The investigations on photocatalytic reaction mechanisms,[5−7] energy-band structure engineering (including the optimization of crystal structure and the modulation of band energy levels),[8−10] and morphology control[11−15] have been carried out to enhance the photocatalytic efficiency. Generally, to study the relationship between crystal structure and electronic structure is helpful to understand the process of photogenerated carrier excitation and transfer. Up to now, the relevant studies have been performed on the TiO_2, CdS, $BiVO_4$, and $AgGaO_2$ with different crystal structures.[16−19] Among intensively studied photocatalysts, the materials with perovskite and multilayered perovskite structures have received considerable attention.[20−24] However, the report about the influence of crystallographic symmetry on photogenerated carrier excitation and transfer in the perovskite-structured photocatalysts is still limited.

$NaNbO_3$ is nontoxic, highly stable, and with a typical perovskite structure and thus attracts extensive attention in the field of photocatalysis. Many investigations have proved that $NaNbO_3$ is a high-efficient photocatalyst for H_2 generation.[25−29] Under the irradiation of high-pressure mercury lamp, H_2O can be reduced into H_2 with quite high efficiency over $NaNbO_3$ nanoparticles.[29] Nanofiber-structured $NaNbO_3$ was also verified to be useful to slit pure water and reduce CO_2 to CH_4.[30] Moreover, $NaNbO_3$ normally belongs to the orthorhombic system at room temperature and exhibits an unusual complex sequence of temperature-, pressure-, and particle-size-driven phase transitions.[31−35] When the temperature ranges from room temperature to 1000 K, there are several other phases of $NaNbO_3$ existing, such as tetragonal and cubic structures.[36] All of them, cubic, tetragonal, and orthorhombic $NaNbO_3$, are constructed from a basic perovskite unit. However, to the best of our knowledge, all the reported photocatalytic measurements were carried out over the common orthorhombic $NaNbO_3$ and no measurement has been done over the other phases of $NaNbO_3$. Fabricating the $NaNbO_3$ with different crystal structures will help us to understand the influence of the crystallographic symmetry in the perovskite structure on the electronic structures and photocatalytic properties. Hence, in this work, cubic $NaNbO_3$ (c-$NaNbO_3$) and orthorhombic $NaNbO_3$ (o-$NaNbO_3$) were selectively synthesized.

Received: October 21, 2011
Revised: January 30, 2012
Published: March 11, 2012

   dx.doi.org/10.1021/jp210106b | J. Phys. Chem. C 2012, 116, 7621−7628

The photocatalytic properties of these materials were characterized using the photocatalytic H_2 evolution and CO_2 photoreduction under UV−visible light irradiation. Detailed studies on the electronic structures were performed to understand the difference of photocatalytic activity between the c-$NaNbO_3$ and o-$NaNbO_3$.

EXPERIMENTAL SECTION

Material Preparation. The c-$NaNbO_3$ was synthesized via a typical furfural alcohol derived polymerization−oxidation (FAPO) process.[37] First, 1.0 g of $(C_2H_5O)_5Nb$ and 0.24 g of C_2H_5ONa were added into 10 mL of 2-methoxyethanol and stirred at room temperature to form a clear colloid. After that, 2.5 g of P-123 (M_w = 5800) dissolved in 30 mL of furfuryl alcohol was added. Next, the mixture was stirred for 30 min and then heated to 95 °C with a rate of 1 °C·min^{-1} and maintained at this temperature for 120 h in air to form a black solid polymer. Finally, the black solid was oxidized in air at 600 °C for 5 h, and a white powder product was obtained. To synthesize o-$NaNbO_3$ by a polymerized complex (PC) method,[29] 1.0 g of $NbCl_5$ and 0.20 g of Na_2CO_3 were added into 10 mL of ethanol and stirred at room temperature to form a clear colloid. This colloid was then added into 50 mL of ethanol solution containing 12.0 g of critic acid and 2.0 mL of ethylene glycol. After it was stirred for 30 min, the mixture was heated to 120 °C with a rate of 1 °C·min^{-1} and maintained at this temperature for 20 h in air for polymerization. Finally, the polymer was oxidized in air at 600 °C for 2 h, and a white powder product was obtained.

Sample Characterization. The crystal structure of $NaNbO_3$ powder was determined with an X-ray diffractometer (Rint-2000, Rigaku Co., Japan) with Cu Kα radiation. The diffuse reflection spectra were measured with an integrating sphere equipped UV−visible recording spectrophotometer (UV-2500PC, Shimadzu Co., Japan) using $BaSO_4$ as a reference, and the optical absorptions were converted from the reflection spectra according to the Kubelka−Munk equation. The specific surface areas were determined with a surface-area analyzer (BEL Sorp-II mini, BEL Japan Co., Japan) by the Brunauer−Emmett−Teller (BET) method. Transmission electron microscopy images and high-resolution images were recorded with a field emission transmission electron microscope (2100F, JEOL Co., Japan) operated at 200 kV. X-ray photoelectron spectroscopy (XPS) experiments were performed in type Theta probe (Thermo Fisher Co.) using monochromatized Al Kα at $h\nu$ = 1486.6 eV, and the peak positions were internally referenced to the C 1s peak at 284.6 eV.

Photocatalytic H_2 Evolution. The H_2 evolution experiments were carried out in a gas closed circulation system. The $NaNbO_3$ powder (0.3 g) was dispersed by using a magnetic stirrer in CH_3OH aqueous solution (220 mL of distilled water + 50 mL of CH_3OH) in a Pyrex cell with a side window. The 0.5−1.5 wt % of Pt cocatalyst was photodeposited on the $NaNbO_3$ catalyst by adding a calculated amount of H_2PtCl_6 solution into the reaction solution. The light source was a 300 W Xe arc lamp without a filter (λ > 300 nm). The H_2 evolution was measured with an online gas chromatograph (GC-8A, Shimadzu) with a thermal conductivity detector (TCD) according to the standard curve. After the H_2 evolution persisted for 8 h, the resulting $NaNbO_3$ powder was separated by centrifugation and washed with the distilled water for several times. The sample was then dried in vacuum at 250 °C and continually heated at 400 °C for 3 h to remove organic compounds adsorbed on the surface of the catalyst. The obtained sample with Pt loaded was further tested for the photoactivity of CO_2 reduction.

CO_2 Photoreduction. The CO_2 photoreduction experiments were carried out in a gas closed circulation system with an upside window. The Pt-loaded catalyst powder (0.1 g) was dispersed on a small glass cell and then located in a Pyrex reaction cell. After that, 3 mL of distilled water was added into the gas closed reaction system. The whole system was then evacuated and filled with 80 kPa of pure CO_2 gas. The light source was a 300 W Xe arc lamp without a filter. The organic products were sampled and measured with a gas chromatograph (GC-14B, Shimadzu) equipped with a flame ionization detector (FID) according to the standard curves. The H_2 evolution was measured with an online gas chromatograph (GC-8A, Shimadzu) with a TCD detector according to the standard curve.

Theoretical Calculation. The band structures, densities of state (DOS), and partial densities of state (PDOS) of cubic and orthorhombic $NaNbO_3$ were calculated using the plane-wave density functional theory (DFT) with the CASTEP program package.[38] The core electrons were replaced by ultrasoft pseudopotentials with a plane-wave basis cutoff energy of 370 eV, and the interactions of exchange and correlation were treated within the framework of the local density approximation (LDA). The FFT grids of basis in all the models were 24 × 24 × 24 and 32 × 90 × 30 for c-$NaNbO_3$ and o-$NaNbO_3$, respectively. The *k*-point sets of 6 × 6 × 6 for c-$NaNbO_3$ and 5 × 2 × 5 for o-$NaNbO_3$ were used.

RESULTS AND DISCUSSION

Crystal Structure. The basic perovskite $NaNbO_3$, which has a cubic structure with the space group of $Pm\bar{3}m$ (Figure 1),

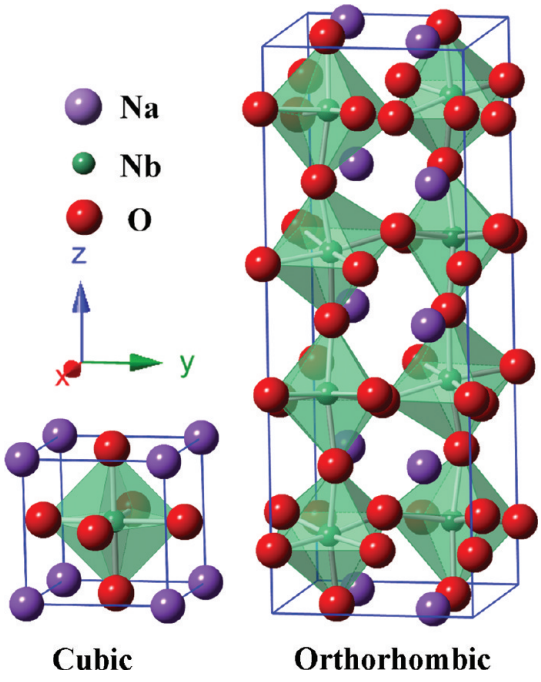

Figure 1. Schematic crystal structures of cubic and orthorhombic $NaNbO_3$.

is only stable at high temperature (>913 K).[31,36] When cooling down from high temperature, $NaNbO_3$ undergoes a series of phase transitions from cubic to rhombohedral via intermediate tetragonal and orthorhombic phases. At room temperature, the common phase of $NaNbO_3$ is an antiferroelectric orthorhombic

dx.doi.org/10.1021/jp210106b | J. Phys. Chem. C 2012, 116, 7621−7628

phase, space group of *Pbcm*, a = 5.506 Å, b = 5.566 Å, and c = 15.52 Å (Figure 1).[39] This phase processes an "octahedral tilting" with three independent tilts as a $\sqrt{2}a_0 \times \sqrt{2}a_0 \times 4a_0$ supercell of the basic cubic perovskite cell, where a_0 is the cubic lattice parameter, 3.906 Å.[40]

The crystallographic phases of as-prepared $NaNbO_3$ were determined by X-ray diffraction (XRD) (Figure 2). The patterns

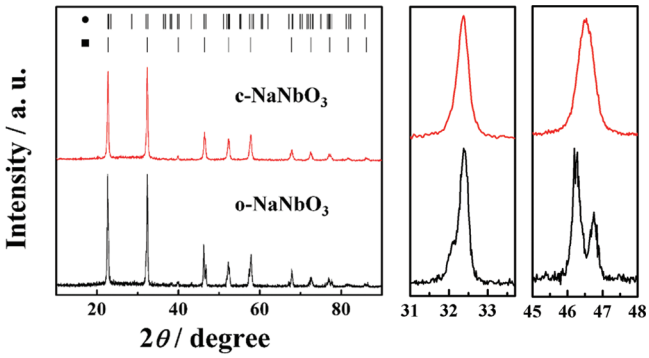

Figure 2. XRD patterns of the as-prepared $NaNbO_3$ samples (●, orthorhombic; ■, cubic).

show that the $NaNbO_3$ prepared through the FAPO route crystallized in a cubic system with the space group of $Pm\bar{3}m$, whereas the $NaNbO_3$ synthesized by a PC method was formed in an orthorhombic system with the space group of *Pbcm*. The diffraction peaks, of which 2θ are about 32.5° and 46.5°, show the obvious difference between cubic and orthorhombic $NaNbO_3$. All peaks in these patterns could be indexed to the JCPDS database card (JCPDS-075-2102 for cubic and JCPDS-073-0803 for orthorhombic). Because the surface energy of c-$NaNbO_3$ is higher than that of o-$NaNO_3$, by common synthetic methods, the orthorhombic phase favors to form at room temperature.[32,41] The formation of c-$NaNbO_3$ by a FAPO method is probably attributed to the addition of the surfactant P-123, which stabilized the surface of the c-$NaNbO_3$ crystal in solution. The study of the detailed mechanism of crystal growth is under way. The average crystallite sizes of c-$NaNbO_3$ and o-$NaNbO_3$ were calculated to be 18.5 and 23.1 nm using the Debye−Scherrer equation. The lattice parameters of $NaNbO_3$ were refined by the least-squares method (as listed in Table 1).

Transmission electron microscopy (TEM) and high-resolution transmission electron microscopy (HR-TEM) were further used to confirm the crystal structures of the as-prepared samples (Figure 3). The c-$NaNbO_3$ sample is constituted by particles with a uniform cuboid morphology. The cuboids are generally 40 nm in length. The o-$NaNbO_3$ sample contains irregular and cuboid particles. As exhibited in Figure 3b, the c-$NaNbO_3$ sample exhibits two mutually perpendicular fringes with the same d-spacing, 3.91 Å, which could be indexed to the

Table 1. Crystal Structures and Photophysical and Photocatalytic Properties of $NaNbO_3$

materials	crystal systems	lattice parameters (Å)	band gaps (eV)	surface areas ($m^2 \cdot g^{-1}$)	H_2 evolution ($\mu mol \cdot h^{-1}$)	CH_4 evolution ($\mu mol \cdot h^{-1}$)
c-$NaNbO_3$	cubic	a = 3.909(2)	3.29	28.6	127	0.486
o-$NaNbO_3$	orthorhombic	a = 5.577(3), b = 5.524(3), c = 15.579(7)	3.45	26.4	72.3	0.245

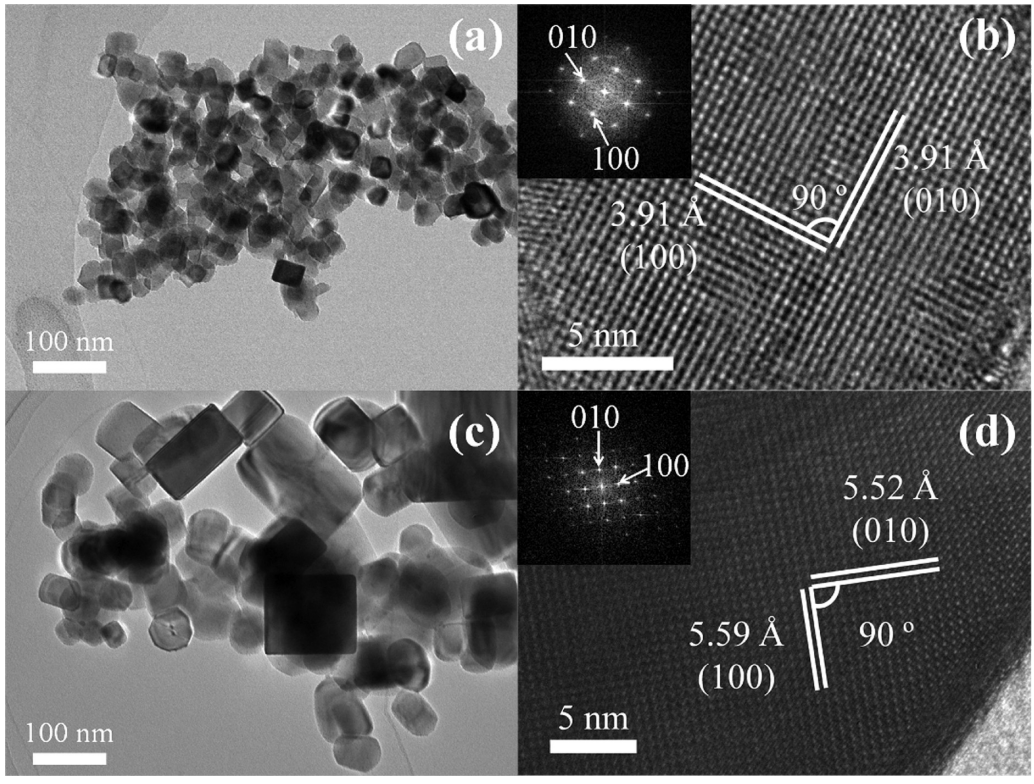

Figure 3. TEM (a) and HR-TEM (b) images of c-$NaNbO_3$. TEM (c) and HR-TEM (d) images of o-$NaNbO_3$. The insets are the corresponding FFT patterns of two samples.

dx.doi.org/10.1021/jp210106b | J. Phys. Chem. C 2012, 116, 7621−7628

{010} and {100} plane of c-$NaNbO_3$. From Figure 3d, two sets of orthorhombic fringes with lattice spacings of 5.52 and 5.59 Å are observed, corresponding to the {010} and {100} planes of o-$NaNbO_3$, respectively. The insets of Figure 3b,d give the corresponding fast Fourier transform (FFT) patterns of two samples, which show the clear evidence to distinguish the two phases. The BET surface areas were measured to be 28.6 and 26.4 $m^2 \cdot g^{-1}$ for c-$NaNbO_3$ and o-$NaNbO_3$, respectively.

Photophysical Property. UV−visible absorption spectra of c-$NaNbO_3$ and o-$NaNbO_3$ powder samples are shown in Figure 4. Both the two samples have the only intense absorption

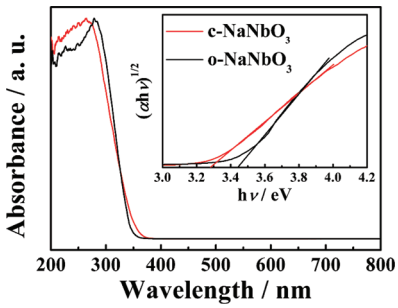

Figure 4. UV−vis absorption spectra of the as-prepared $NaNbO_3$ samples. The inset is the corresponding $(\alpha h\nu)^{1/2}-h\nu$ curves.

with steep edges in the UV region. Compared with the absorption edge of o-$NaNbO_3$, that of c-$NaNbO_3$ has a slight red shift, suggesting that the c-$NaNbO_3$ could absorb longer wavelength light. The band gaps (E_g) of c-$NaNbO_3$ and o-$NaNbO_3$ were determined according to the following equation

$$(\alpha h\nu)^n = A(h\nu - E_g)$$

in which α, ν, A, and E_g are the absorption coefficient, light frequency, proportionality constant, and band gap, respectively.[42] The value of index n depends on the property of materials, where $n = 2$ for the direct-band-gap semiconductor and $n = 1/2$ for the indirect-band-gap semiconductor.[42] For both $NaNbO_3$ samples, the indexes n were determined to be 1/2 according to the relationship between $\log(\alpha h\nu)$ and $\log(h\nu - E_g)$. From the inset of Figure 4, the values of the band gaps for c-$NaNbO_3$ and o-$NaNbO_3$ are determined to be 3.29 and 3.45 eV, respectively. The c-$NaNbO_3$ sample possesses a narrower band gap than o-$NaNbO_3$.

H_2 Evolution Activity. The H_2 evolutions from CH_3OH aqueous solution (50 mL of CH_3OH + 220 mL of H_2O) over 0.5 wt % of Pt-loaded powder catalysts (0.3 g) under the irradiation of a Xe lamp ($\lambda > 300$ nm) are presented in Figure 5a. As mentioned previously, both the cubic and the orthorhombic $NaNbO_3$ are constructed of a basic perovskite structure. However, their photocatalytic activities are significantly different: c-$NaNbO_3$ > o-$NaNbO_3$. The H_2 evolution amounts increased almost linearly in 8 h and were about 127 and 72.3 $\mu mol \cdot h^{-1}$ for c-$NaNbO_3$ and o-$NaNbO_3$, respectively. The difference in the photocatalytic activity between c-$NaNbO_3$ and o-$NaNbO_3$ is probably attributed to their different electronic structures and will be discussed in the following section.

For H_2 evolution, the Pt serves as a cocatalyst to supply the reactive site where H_2 could generate easily due to the low H_2 overpotential on the Pt surface. The loaded Pt cocatalysts largely affect the H_2 generation efficiency. The photocatalytic performance is influenced by the cover ratio and size of the

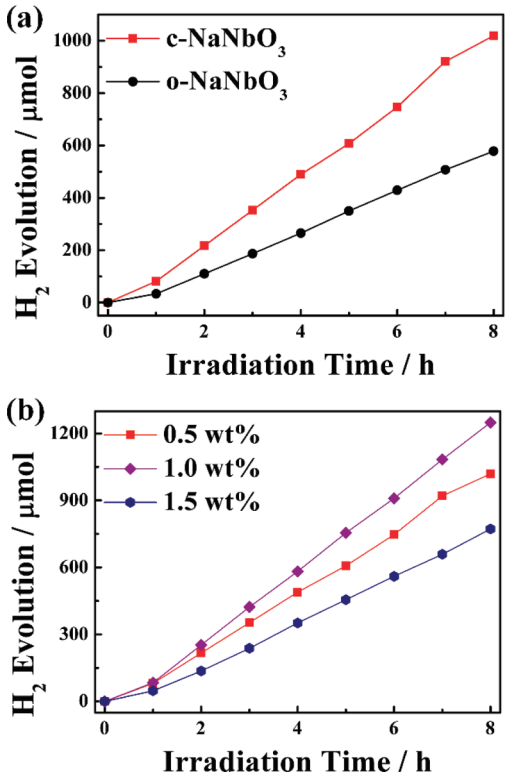

Figure 5. (a) Photocatalytic H_2 evolution from the aqueous methanol solution over c-$NaNbO_3$ and o-$NaNbO_3$ samples with a loading of 0.5 wt % Pt. (b) Photocatalytic H_2 evolution from the aqueous methanol solution over c-$NaNbO_3$ samples with 0.5, 1.0, and 1.5 wt % Pt loaded.

cocatalyst that could be adjusted by the loading amount.[43] Since the c-$NaNbO_3$ sample possessed a special morphology with a relatively high surface area, the optimization of the Pt cocatalyst was performed carefully in this study. The 0.5, 1.0, and 1.5 wt % of Pt cocatalyst were deposited on the c-$NaNbO_3$ surface, and their corresponding photocatalytic H_2 evolutions are plotted in Figure 5b. The H_2 evolution rates over c-$NaNbO_3$ were 127.4, 156.1, and 97.3 $\mu mol \cdot h^{-1}$ for 0.5, 1.0, and 1.5 wt % of Pt loading, respectively. The 1.0 wt % of loading amount supplied a proper cover ratio and size of cocatalyst and hence induced the highest H_2 evolution rate for the c-$NaNbO_3$ photocatalyst.

CO_2 Photoreduction Activity. The photoreductive ability of $NaNbO_3$ could also be applicable for converting CO_2 into useful organic fuels, such as CH_4. Figure 6a exhibits CH_4 generation from CO_2 photoreduction over c-$NaNbO_3$ and o-$NaNbO_3$ with a loading of 0.5 wt % Pt. The CH_4 evolution rates over c-$NaNbO_3$ and o-$NaNbO_3$ were determined to be 0.486 and 0.245 $\mu mol \cdot h^{-1}$, respectively. The photoactivity order is the same as that of the H_2 evolution reaction, c-$NaNbO_3$ > o-$NaNbO_3$. The optimization of the loading amount of Pt cocatalyst was also carried out for CO_2 photoreduction. The 1.0 wt % of Pt-loaded c-$NaNbO_3$ photocatalyst showed the best photocatalytic activity, which is in good agreement with the H_2 evolution result (Figure 6b). These results reveal that the processes of electron excitation and transfer are similar in these two kinds of reactions.

It is well known that the CO_2 photoreduction mainly undergoes two courses, including oxidation and reduction processes. In the oxidation process, H_2O is oxidized to O_2 ($2H_2O + 4h^+ \rightarrow O_2 + 4H^+$). In the reduction course, there is a chain reaction to

dx.doi.org/10.1021/jp210106b | J. Phys. Chem. C 2012, 116, 7621−7628

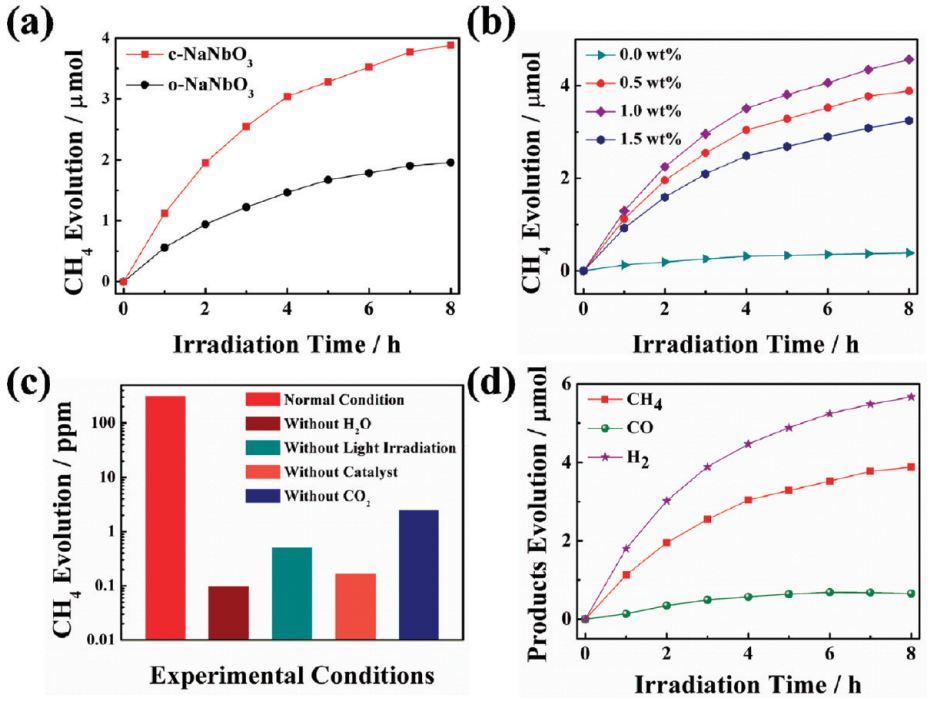

Figure 6. (a) CH_4 evolution in gas-phase reaction over c-$NaNbO_3$ and o-$NaNbO_3$ samples (with loading 0.5 wt % Pt). (b) CH_4 evolution over c-$NaNbO_3$ samples with 0.0, 0.5, 1.0, and 1.5 wt % Pt loaded. (c) CH_4 evolution in reference experiments in the condition without H_2O, CO_2, light irradiation, and catalyst compared with that in normal conditions. (d) CH_4, CO, and H_2 evolution in gas-phase reaction over 0.5 wt % Pt loaded c-$NaNbO_3$ sample.

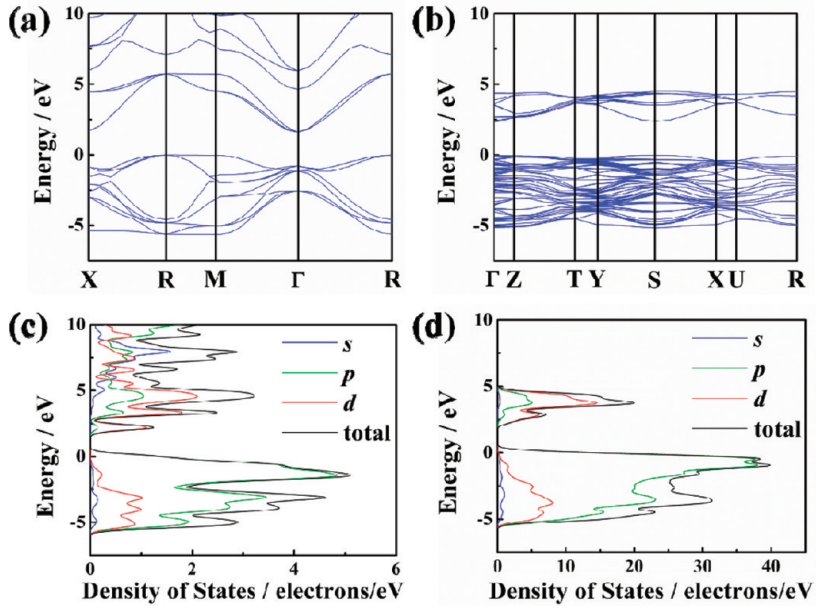

Figure 7. Calculated band structures of c-$NaNbO_3$ (a) and o-$NaNbO_3$ (b). The DOS of c-$NaNbO_3$ (c) and o-$NaNbO_3$ (d).

reduce CO_2 to CH_4 ($CO_2 + 2H^+ + 2e^- \rightarrow HCOOH$, $HCOOH + 2H^+ + 2e^- \rightarrow HCHO + H_2O$, $HCHO + 2H^+ + 2e^- \rightarrow CH_3OH$, $CH_3OH + 2H^+ + 2e^- \rightarrow CH_4 + H_2O$).[44] To confirm that the CH_4 was generated from the photoreduction reaction, reference experiments were carried out over c-$NaNbO_3$. Figure 6c shows the concentration of CH_4 evolution when the reference experiments were carried out for 8 h. When the experiment was carried out in the absence of H_2O, only 0.1 ppm of CH_4 was detected. In the absence of catalyst or light irradiation, there were merely 0.33 and 0.15 ppm of CH_4, respectively. Since there is about 1 ppm of CH_4 in the natural air, the CH_4 in the above-mentioned experiments is considered as the contamination from air during samplings. Nevertheless, in the case that the CO_2 gas was replaced by Ar gas, 1.2 ppm of CH_4 was found. This value is obviously higher than that in natural air. As the sample was prepared from a carbon-containing precursor and $NaNbO_3$ possesses an alkaline surface, it is difficult to remove all the CO_2 from the sample surface even after a long calcination time. We once tested the CO_2 amount in the reaction system during the reference experiment without CO_2

dx.doi.org/10.1021/jp210106b | J. Phys. Chem. C 2012, 116, 7621−7628

and found that about 300 ppm of CO_2 evolved from the sample surface. Therefore, a small amount of CH_4 should be generated from the photoreduction of the remaining CO_2 on the sample surface. Consequently, all the above-mentioned reference experiments prove that the H_2O supplies protons, CO_2 offers a carbon source, and the photocatalyst gives the redox potentials for the whole reaction to finally produce CH_4.

Besides CH_4, other hydrocarbon compounds (C_2H_4, C_2H_6, and C_3H_8) were also generated in the reaction. However, the productions of these organic compounds were much lower than that of CH_4. This results suggest that the long chain organic molecules are generated via photocatalytic reforming of CH_4, and CH_4 is the source of this reaction.[45,46] Inorganic byproducts CO and H_2 were also detected, as shown in Figure 6d. CO is a common byproduct in the CO_2 reduction. Along with the CO_2 reduction over c-$NaNbO_3$, CO was produced with the rate of 0.082 μmol·h^{-1}. Although the reduction potential of H_2O to H_2 (−0.41 V vs NHE, pH = 7) is more negative than that of CO_2 to CH_4 (−0.24 V vs NHE, pH = 7),[44] the evolution rate of H_2 (0.71 μmol·h^{-1}) was higher than that of CH_4 (0.486 μmol·h^{-1} catalyst). This could be attributed to that more electrons are consumed in CO_2 reduction (CO_2 + $6H_2O$ + $8e^- \rightarrow CH_4 + 8OH^-$) than those in H_2O reduction ($2H_2O + 2e^- \rightarrow H_2 + 2OH^-$). Thus, the H_2 is easier to be generated dynamically.

Table 2. Optimized Bond Lengths and Bond Angles of $NaNbO_3$

	Nb−O bond length (Å)	O−Nb−O bond angle (degree)
c-$NaNbO_3$	1.966	90.00
o-$NaNbO_3$	1.971 (a−o)	86.13 (a−o−c) 93.65 (a−o−d)
	1.974 (b−o)	85.84 (a−o−e) 93.28 (a−o−f)
	2.084 (c−o)	86.73 (b−o−c) 93.47 (b−o−d)
	1.895 (d−o)	86.33 (b−o−e) 93.14 (b−o−f)
	2.075 (e−o)	89.27 (c−o−d) 84.82 (c−o−e)
	1.892 (f−o)	96.20 (f−o−d) 89.71 (f−o−e)

Electronic Structure. The crystal structures of c-$NaNbO_3$ and o-$NaNbO_3$ are constructed of the same basic perovskite unit. Moreover, the band gap difference between the two materials is less than 0.2 eV. However, the photocatalytic H_2 generation and CO_2 reduction activities of c-$NaNbO_3$ are severely higher than those of o-$NaNbO_3$. Thus, the detailed investigation on band structure was carried out to understand this experimental phenomenon. The DFT calculation was used to investigate the electronic structures of c-$NaNbO_3$ and o-$NaNbO_3$. Figure 7a,b shows the calculated band structures of c-$NaNbO_3$ and o-$NaNbO_3$, respectively. The band structures indicate that both of them are typical indirect-band-gap semiconductors, which is consistent with the analysis of UV−visible absorption spectra. The theoretical band gaps of c-$NaNbO_3$ and o-$NaNbO_3$ are 1.63 and 2.33 eV, respectively, which are smaller than the values from experimental data. This difference is caused by the limitation of the LDA functional that underestimates the band gaps in semiconductor simulation. Besides the narrower band gap, the conduction bands of c-$NaNbO_3$ are more dispersive than those of o-$NaNbO_3$, which indicates that the photogenerated electrons in c-$NaNbO_3$ possess a smaller effective mass and, therefore, higher migration ability, inducing that c-$NaNbO_3$ shows higher photoreduction activity than o-$NaNbO_3$. Further information is obtained from the DOS and PDOS of c-$NaNbO_3$ and o-$NaNbO_3$ (Figure 7c,d). Both of the valence band tops of c-$NaNbO_3$ and o-$NaNbO_3$ are constructed from O 2p orbitals, and thus, they locate at similar energy levels, which is consistent with the XPS data shown in Figure S1a (Supporting Information). Nevertheless, the conduction band bottoms of c-$NaNbO_3$ and o-$NaNbO_3$ are significantly different. The energy level of the conduction band bottom in c-$NaNbO_3$ is lower than that in o-$NaNbO_3$. This difference is attributed to the variant octahedral ligand field of o-$NaNbO_3$ that changes Nb−O bond lengths and O−Nb−O

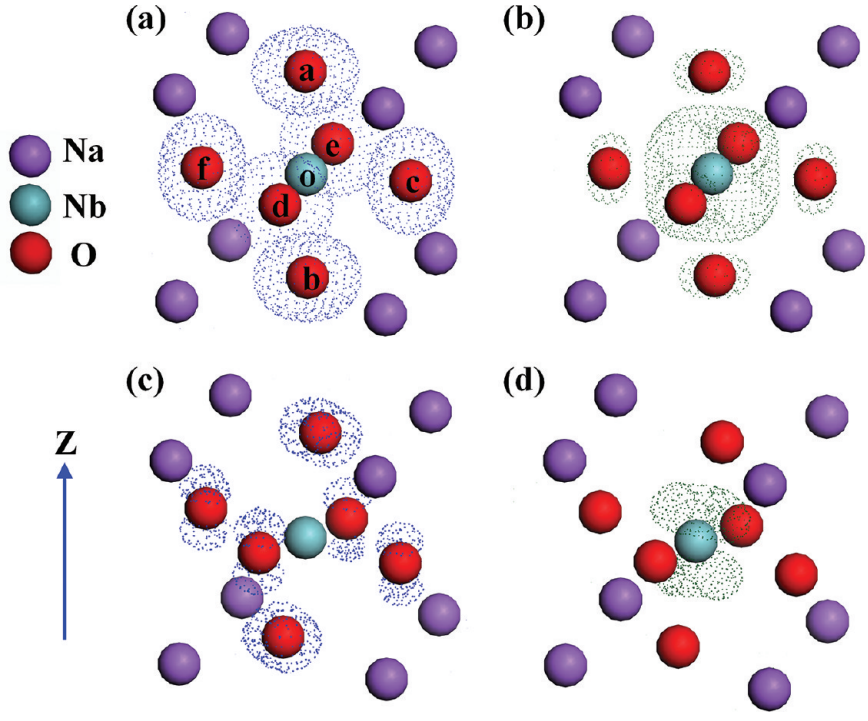

Figure 8. Frontier orbital distributions of $NaNbO_3$: HOMO (a) and LUMO (b) of c-$NaNbO_3$; HOMO (c) and LUMO (d) of o-$NaNbO_3$.

dx.doi.org/10.1021/jp210106b | J. Phys. Chem. C 2012, 116, 7621−7628

bond angles (as listed in Table 2) of the basic cubic crystal structure. When the crystal structure of $NaNbO_3$ changes from cubic to orthorhombic style, the tilts of Nb−O bonds and the shifts of bond lengths contribute to lowering the energy; however, the Nb−O bond lengths in the z direction are nearly the same. Moreover, the frontier orbital distributions also supply the explanation for the photocatalytic activity difference (Figure 8). As the conduction band bottom of c-$NaNbO_3$ possesses a delocalized orbital covering Nb and O atoms, the photogenerated electrons could transfer along the x, y, and z directions isotropically. Nevertheless, for o-$NaNbO_3$ that possesses a localized conduction band bottom, the frontier orbital distributions exhibit a nonisotropy figure, inducing that the photogenerated electrons favor the migration along the z direction other than the x and y directions. Therefore, the high symmetry in the crystal structure of c-$NaNbO_3$ is beneficial for the transfer of photogenerated electrons and, subsequently, the better photoreduction activity.

CONCLUSIONS

In conclusion, cubic and orthorhombic $NaNbO_3$ were synthesized to study the effect of crystallographic symmetry on the electronic structure and photocatalytic activity in the perovskite structure in detail. This c-$NaNbO_3$ shows a narrower bang gap (3.29 eV) than the common o-$NaNbO_3$ (3.45 eV). In photocatalytic H_2 generation, c-$NaNbO_3$ (127 $\mu mol \cdot h^{-1}$) shows higher activity than o-$NaNbO_3$ (72.3 $\mu mol \cdot h^{-1}$). For CO_2 photoreduction in the gas phase, the CH_4 evolution rate over c-$NaNbO_3$ (0.486 $\mu mol \cdot h^{-1}$) is about twice that over o-$NaNbO_3$ (0.245 $\mu mol \cdot h^{-1}$). Theoretical calculation demonstrated that the band gap difference between the two phases of $NaNbO_3$ is caused by the variant octahedral ligand field. Furthermore, the high symmetry in c-$NaNbO_3$ results in its unique electronic structure that is beneficial for the electron excitation and transfer and thus contributes to its higher photocatalytic activity compared with o-$NaNbO_3$. The present study evidences that reforming the crystal structure of the perovskite semiconductor toward a higher symmetry can improve the photoelectron excitation and transfer. Therefore, it offers a new idea to enhance the photocatalytic efficiency in other perovskite or multilayered perovskite photocatalysts.

ASSOCIATED CONTENT

Supporting Information

XPS spectra of as-prepared $NaNbO_3$, XRD patterns and UV−visible absorption spectra of original catalysts and the catalysts after H_2 evolution and CO_2 reduction, and PDOS of Nb 3d and Na 1s orbitals. This material is available free of charge via the Internet at http://pubs.acs.org.

AUTHOR INFORMATION

Corresponding Author

*E-mail: jinhua.ye@nims.go.jp.

Notes

The authors declare no competing financial interest.

ACKNOWLEDGMENTS

This work was partially supported by the World Premier International Research Center Initiative on Materials Nanoarchitectonics, MEXT, and JST-MOST Strategic Japanese-Chinese Cooperative Programme, Japan.

REFERENCES

(1) Hammarstrom, L.; Hammes-Schiffer, S. *Acc. Chem. Res.* **2009**, *42*, 1859.
(2) Gust, D.; Moore, T. A.; Moore, A. L. *Acc. Chem. Res.* **2001**, *34*, 40.
(3) Chen, X.; Shen, S.; Guo, L.; Mao, S. S. *Chem. Rev.* **2010**, *110*, 6503.
(4) Tong, H.; Ouyang, S.; Bi, Y.; Umezawa, N.; Oshikiri, M.; Ye, J. *Adv. Mater.* **2012**, *24*, 229.
(5) Tang, J.; Durrant, J. R.; Klug, D. R. *J. Am. Chem. Soc.* **2008**, *130*, 13885.
(6) Indrakanti, V. P.; Schobert, H. H.; Kubicki, J. D. *Energy Fuels* **2009**, *23*, 5247.
(7) Varley, J. B.; Janotti, A.; Van de Walle, C. G. *Adv. Mater.* **2011**, *23*, 2343.
(8) Ouyang, S. X.; Ye, J. H. *J. Am. Chem. Soc.* **2011**, *133*, 7757.
(9) Umezawa, N.; Shuxin, O. Y.; Ye, J. H. *Phys. Rev. B* **2011**, *83*, 035202.
(10) Li, Y.-F.; Liu, Z.-P.; Liu, L.; Gao, W. *J. Am. Chem. Soc.* **2010**, *132*, 13008.
(11) Diebold, U. *Surf. Sci. Rep.* **2003**, *48*, 53.
(12) Liu, S.; Yu, J.; Jaroniec, M. *J. Am. Chem. Soc.* **2010**, *132*, 11914.
(13) Bi, Y.; Ouyang, S.; Umezawa, N.; Cao, J.; Ye, J. *J. Am. Chem. Soc.* **2011**, *133*, 6490.
(14) Miyauchi, M. *J. Phys. Chem. C* **2007**, *111*, 12440.
(15) Wang, D.; Pierre, A.; Kibria, M. G.; Cui, K.; Han, X.; Bevan, K. H.; Guo, H.; Paradis, S.; Hakima, A.-R.; Mi, Z. *Nano Lett.* **2011**, *11*, 2353.
(16) Kandiel, T. A.; Feldhoff, A.; Robben, L.; Dillert, R.; Bahnemann, D. W. *Chem. Mater.* **2010**, *22*, 2050.
(17) Bao, N.; Shen, L.; Takata, T.; Domen, K.; Gupta, A.; Yanagisawa, K.; Grimes, C. A. *J. Phys. Chem. C* **2007**, *111*, 17527.
(18) Ouyang, S. X.; Kikugawa, N.; Chen, D.; Zou, Z. G.; Ye, J. H. *J. Phys. Chem. C* **2009**, *113*, 1560.
(19) Liu, Y. Y.; Huang, B. B.; Dai, Y.; Zhang, X. Y.; Qin, X. Y.; Jiang, M. H.; Whangbo, M. H. *Catal. Commun.* **2009**, *11*, 210.
(20) Rabuffetti, F. A.; Stair, P. C.; Poeppelmeier, K. R. *J. Phys. Chem. C* **2010**, *114*, 11056.
(21) Wang, D. F.; Kako, T.; Ye, J. H. *J. Am. Chem. Soc.* **2008**, *130*, 2724.
(22) Abe, R.; Higashi, M.; Sayama, K.; Abe, Y.; Sugihara, H. *J. Phys. Chem. B* **2006**, *110*, 2219.
(23) Ebina, Y.; Sakai, N.; Sasaki, T. *J. Phys. Chem. B* **2005**, *109*, 17212.
(24) Wang, D. F.; Ye, J. H.; Kako, T.; Kimura, T. *J. Phys. Chem. B* **2006**, *110*, 15824.
(25) Saito, K.; Kudo, A. *Inorg. Chem.* **2010**, *49*, 2017.
(26) Li, G. Q.; Yang, N.; Wang, W. L.; Zhang, W. F. *J. Phys. Chem. C* **2009**, *113*, 14829.
(27) Katsumata, K.; Okazaki, S.; Cordonier, C. E. J.; Shichi, T.; Sasaki, T.; Fujishima, A. *ACS Appl. Mater. Interfaces* **2010**, *2*, 1236.
(28) Shi, H. F.; Li, X. K.; Wang, D. F.; Yuan, Y. P.; Zou, Z. G.; Ye, J. H. *Catal. Lett.* **2009**, *132*, 205.
(29) Li, G. Q.; Kako, T.; Wang, D. F.; Zou, Z. G.; Ye, J. H. *J. Phys. Chem. Solids* **2008**, *69*, 2487.
(30) Shi, H. F.; Wang, T. Z.; Chen, J.; Zhu, C.; Ye, J. H.; Zou, Z. G. *Catal. Lett.* **2011**, *141*, 525.
(31) Mishra, S. K.; Choudhury, N.; Chaplot, S. L.; Krishna, P. S. R.; Mittal, R. *Phys. Rev. B* **2007**, *76*, 024110.
(32) Shiratori, Y.; Magrez, A.; Dornseiffer, J.; Haegel, F.-H.; Pithan, C.; Waser, R. *J. Phys. Chem. B* **2005**, *109*, 20122.
(33) Denoyer, F.; Lambert, M.; Comes, R.; Currat, R. *Solid State Commun.* **1976**, *18*, 441.
(34) Tomeno, I.; Tsunoda, Y.; Oka, K.; Matsuura, M.; Nishi, M. *Phys. Rev. B* **2009**, *80*, 104101.
(35) Darlington, C. N. W.; Knight, K. S. *Physica B* **1999**, *266*, 368.
(36) Mishra, S. K.; Mittal, R.; Pomjakushin, V. Y.; Chaplot, S. L. *Phys. Rev. B* **2011**, *83*, 134105.
(37) Xi, G. C.; Ouyang, S. X.; Ye, J. H. *Chem.—Eur. J.* **2011**, *17*, 9057.

(38) Segall, M. D.; Lindan, P. J. D.; Probert, M. J.; Pickard, C. J.; Hasnip, P. J.; Clark, S. J.; Payne, M. C. *J. Phys.: Condens. Matter* **2002**, *14*, 2717.
(39) Sakowski-Cowley, A. C.; Lukaszewicz, K.; Megaw, H. D. *Acta Crystallogr., Sect. B* **1969**, *25*, 851.
(40) Barth, T. *Nor. Geol. Tidsskr.* **1925**, *8*, 201.
(41) Johnston, K. E.; Tang, C. C.; Parker, J. E.; Knight, K. S.; Lightfoot, P.; Ashbrook, S. E. *J. Am. Chem. Soc.* **2010**, *132*, 8732.
(42) Butler, M. A. *J. Appl. Phys.* **1977**, *48*, 1914.
(43) Yin, J.; Zou, Z.; Ye, J. *J. Phys. Chem. B* **2004**, *108*, 12790.
(44) Inoue, T.; Fujishima, A.; Konishi, S.; Honda, K. *Nature* **1979**, *277*, 637.
(45) Yuliati, L.; Hattori, T.; Itoh, H.; Yoshida, H. *J. Catal.* **2008**, *257*, 396.
(46) Yuliati, L.; Hattori, T.; Yoshida, H. *Phys. Chem. Chem. Phys.* **2005**, *7*, 195.